ACSNANO

www.acsnano.org

ARTICLE

Laser Crystallization of Organic–Inorganic Hybrid Perovskite Solar Cells

Taewoo Jeon,[†] Hyeong Min Jin,[†] Seung Hyun Lee,[‡] Ju Min Lee,[†] Hyung Il Park,[†] Mi Kyung Kim,[†] Keon Jae Lee,[‡] Byungha Shin,*[,‡] and Sang Ouk Kim*[,†]

[†]National Creative Research Initiative Center for Multi-Dimensional Directed Nanoscale Assembly, Department of Materials Science and Engineering, KAIST, Daejeon 34141, Republic of Korea

[‡]Department of Materials Science and Engineering, KAIST, Daejeon 34141, Republic of Korea

Supporting Information

ABSTRACT: **Organic–inorganic hybrid perovskites attract enormous research interest for next generation solar energy harvest. Synergistic crystalline structures comprising organic and inorganic components enable solution processing of perovskite films. A reliable crystallization method for perovskites, compatible with fast continuous process over large-area flexible substrates, is crucial for high performance solar cell production. Here, we present laser crystallization of hybrid perovskite solar cells using near-infrared (NIR) laser (λ = 1064 nm). Crystalline morphology of $CH_3NH_3PbI_3$ ($MAPbI_3$) perovskite films are widely controllable with laser irradiation condition while maintaining film uniformity. Photothermal heating effectively assisted by interfacial photoconversion layers is critical for phase transformation without beam damage of multilayered device structures. Notably, laser crystallization attains higher device performances than conventional thermal annealing. Fast laser crystallization with manufacture level scan rate (1 m min^{-1}) demonstrates inverted-type perovskite solar cells with 11.3 and 8.0% efficiencies on typical glass and flexible polymer substrates, respectively, without rigorous device optimization.**

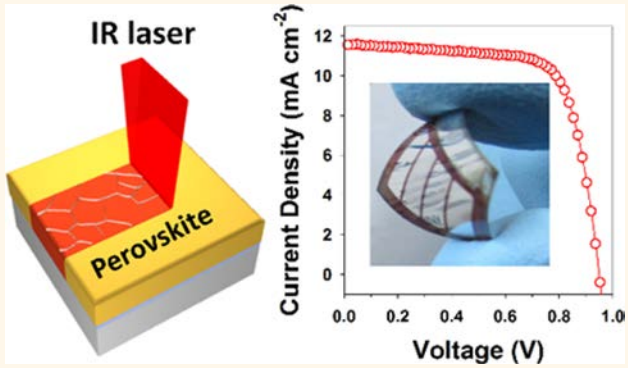

KEYWORDS: *perovskite, laser, crystallization, solar cells, flexible*

Organic–inorganic halide perovskites have emerged as promising materials for optoelectronics,[1,2] particularly photovoltaics.[3−8] Unlike typical oxide perovskites with a large band-bap (3.0–5.0 eV),[9] organic–inorganic hybrid perovskites offer enormous advantages, including optimal band gap for visible spectrum (1.2–3.0 eV),[10−12] high absorption coefficient (as high as 10^5 cm^{-1} order),[13] low exciton binding energy (<50 meV),[14−16] long electron/hole diffusion length,[17] and shallow trap levels.[18] While organic precursors enable solution-processing, soft mechanical properties, and structural diversity of the perovskite layers, the inorganic counterpart facilitates high charge carrier mobility, low exciton binding energy and stability. Since the first report on perovskite solar cells with 3.8% efficiency by Miyasaka et al. in 2009,[19] a considerable amount of research efforts has been devoted to the optimal material compositions,[20,21] device architectures (mesoporous and planar),[22−26] and processing methods for high performance solar cells.[4] It is now well recognized that the key factor for reliable device performance is effective processing of the high crystalline perovskite structures with uniform film morphology.

Along with current technological trend toward flexible and wearable devices, a robust crystallization method for large area flexible substrates is becoming more and more significant. Laser crystallization is a winning candidate for such a purpose owing to the generic competitiveness such as area-selective rapid processing, minimal influence on nonradiated surrounding area, and scalability to continuous large-area processing.[27,28] Effective phase transition of inorganic materials such as amorphous silicon and metal oxides into highly crystalline structures is now well-established based on high energy excimer laser source in UV wavelength regime.[29,30] Such benefits from laser processing coincide with the technological demands for practical perovskite solar cell fabrication. Unfortunately, intensive UV radiation may induce significant damage of the organic components because UV laser carries higher energy than typical bond dissociation energies of organic materials (2–3.6 eV).[31,32] Indeed, methylammonium iodide (MAI), one of the

Received: June 9, 2016
Accepted: June 30, 2016
Published: July 4, 2016

DOI: 10.1021/acsnano.6b03815
ACS Nano 2016, 10, 7907–7914

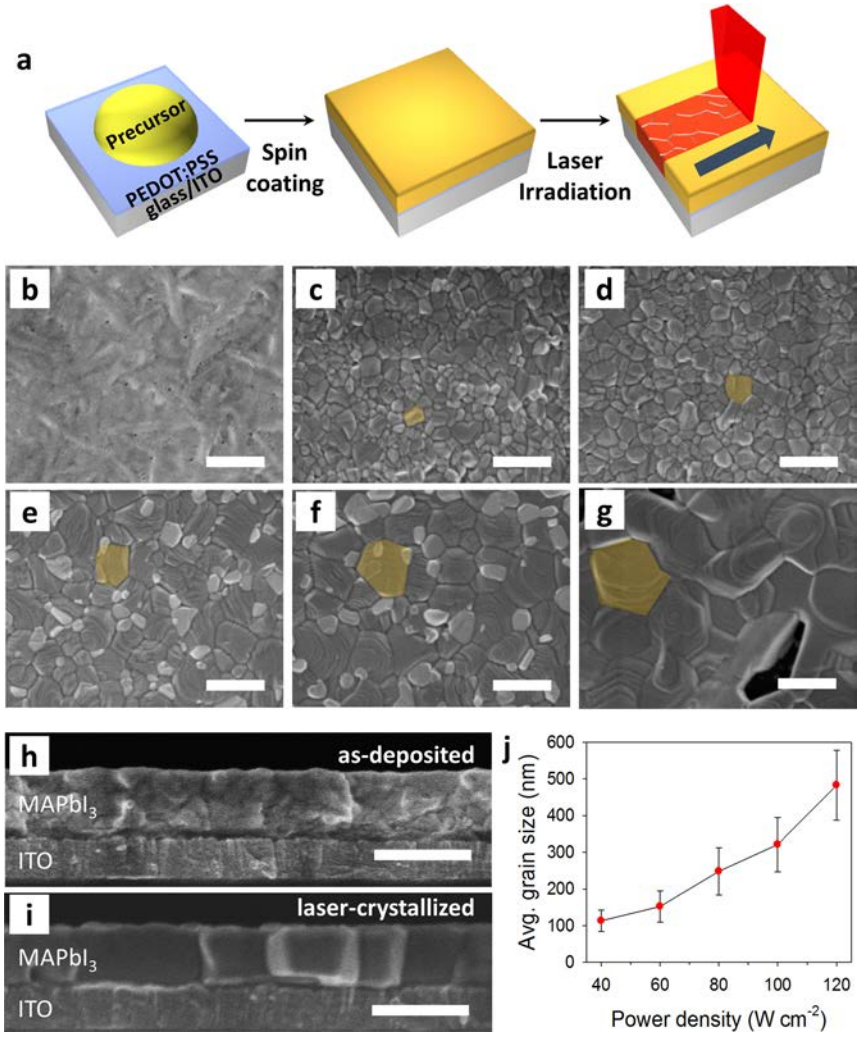

Figure 1. (a) Schematic description of perovskite film formation process. Precursor solution was spread onto PEDOT:PSS coated glass/ITO substrate. Thin-film was formed by spin-coating. Then, the film is exposed to laser beam scan. SEM images of (b) as-coated, (c) 40 W cm^{-2}, (d) 60 W cm^{-2}, (e) 80 W cm^{-2}, (f) 100 W cm^{-2}, and (g) 120 W cm^{-2} with laser power density (scale bar: 500 nm). Cross-sectional SEM images of planar perovskite solar cells with (h) as-deposited and (i) laser-crystallized by 80 W cm^{-2} of laser power density (scale bar: 500 nm). (j) Average grain size as a function of laser power density.

popular precursors for perovskite solar cells, is known to degrade under UV radiation.[33] Besides, a UV laser may interact with transparent conductive oxides (TCO) such as indium tin oxides (ITO) and fluorine-doped tin oxide (FTO) and result in the modification of bonding characteristics and excessive heat generation.[34−36]

In this work, we introduce controllable crystallization of organic−inorganic hybrid perovskite solar cells utilizing low energy NIR laser. ND:YAG laser with a wavelength of 1064 nm is employed for the crystallization of $MAPbI_3$ perovskite solar cells without beam damage. Direct irradiation of the laser beam onto a perovskite precursor layer formed on poly(3,4-ethylenedioxythiophene) polystyrenesulfonate (PEDOT:PSS)-coated ITO induces an instantaneous phase transformation into uniform polycrystalline films with large grain sizes ranging from 100 to 500 nm. Power conversion efficiencies (PCEs) of 11.3 and 8.0% are readily attained with inverted structure perovskite solar cells on glass and flexible substrates, respectively, employing fast laser crystallization under ambient conditions.

RESULTS AND DISCUSSION

Figure 1a schematically illustrates the laser crystallization of perovskite solar cells consisting of the $MAPbI_3$ thin films deposited by single step solution process. Mixture precursor solutions including MAI and lead(II) iodide (PbI_2) are spin-coated onto glass/ITO/PEDOT:PSS substrates under chlorobenzene dripping.[4] A 1064 nm Nd:YAG laser beam is laterally scanned at the film surface and triggers an immediate transformation of the transparent precursor film into dark brown film (Figure S1), indicating the transition of poorly crystalline as-deposited film into light-absorbing perovskite crystalline structure. The resultant film morphology strongly depends on laser irradiation parameters, such as power density and scan rate. Figure 1b−g shows scanning electron microscope (SEM) images of the perovskite film obtained from various laser power densities from 0 to 120 W cm^{-2} with scan rate of 0.1 mm s^{-1}. The low crystalline phase of as-deposited perovskite precursor with branched needles readily transforms into polycrystalline morphology. The grain size increases with power density. Above 80 W cm^{-2}, PbI_2 phase is observed (bright contrast in SEM images) due to the thermal

DOI: 10.1021/acsnano.6b03815
ACS Nano 2016, 10, 7907−7914

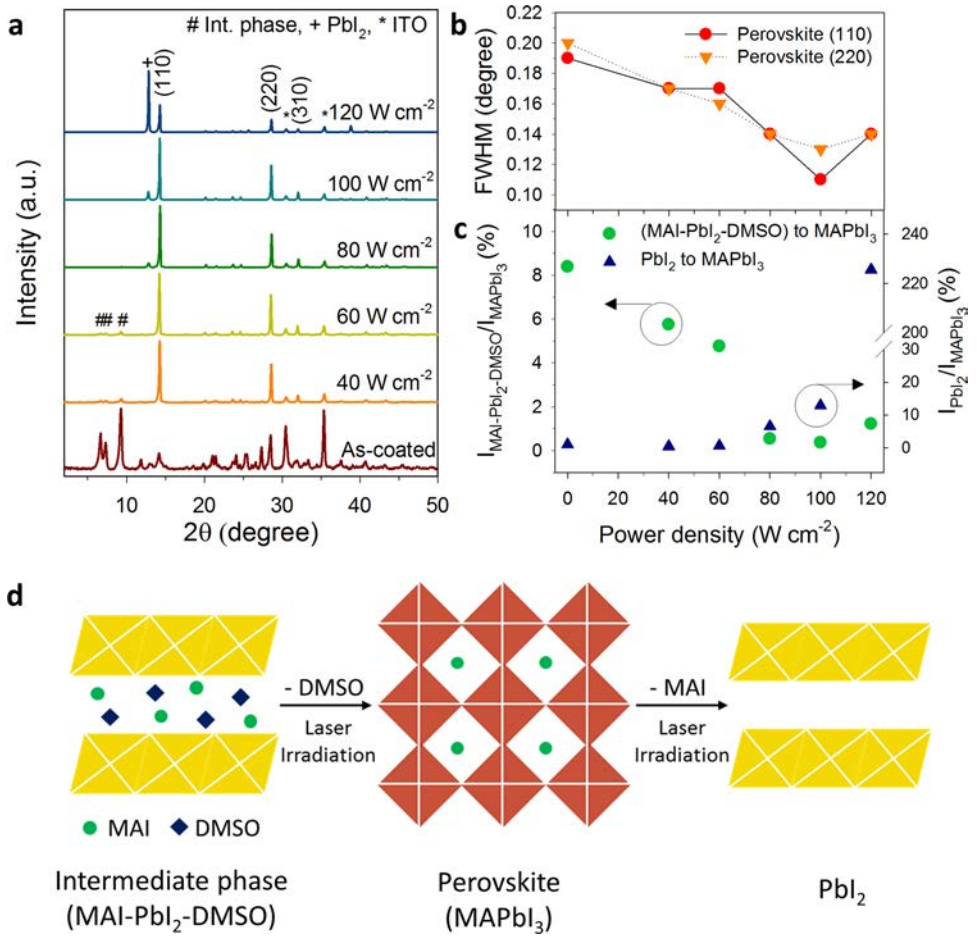

Figure 2. (a) X-ray diffraction (XRD) of laser-crystallized perovskite films at laser power densities. Along with laser power density, (b) Full width at half-maximum (fwhm) values of perovskite (110) and (220) lattice planes and (c) relative peak intensity ratios of intermediate phase (9.3°) and lead(II) iodide (12.8°) to $MAPbI_3$ perovskite (110) plane (14.2°) represented by green circle and blue triangle, respectively. (d) Schematic illustration of the phase transition induced by laser irradiation.

decomposition of the $MAPbI_3$ phase.[37] The average grain size is typically controllable from 100 to 500 nm (Figure 1j). Laser scan rate is another significant parameter for grain growth. A low scan rate delivers a high energy at the same power density resulting in a large crystalline grain size (Figure S2). Figure 1h and i contrast the SEM cross section images of the as-deposited and laser-crystallized perovskite layers. As-deposited film lacks well-defined grain structure, whereas laser crystallization induces clear distinction of perovskite grains throughout the entire film thickness (Figure 1i). An insufficient power density yields small grains with many grain boundaries both in horizontal and vertical directions to the substrate (Figures S3a and S3b). By contrast, sufficient high power density (typically 80 W cm^{-2}) induces large grains with much less boundaries (Figures S3c and S3d). A further increase in the power density over 80 W cm^{-2} causes nonuniform film morphology (Figure S3e).

Figure 2a presents X-ray diffraction (XRD) patterns of the perovskite films treated with different laser power densities. As-deposited perovskite layer shows intermediate peaks under 10 degree as well as weak (110), (220), and (310) lattice plane peaks of tetragonal $MAPbI_3$.[4] Subsequent laser irradiation results in the drastic changes of XRD patterns. Tetragonal $MAPbI_3$ peaks for (110), (220), and (310) lattice planes become clear. The weak intermediate peaks remain up to 60 W cm^{-2}. Meanwhile, PbI_2 peak begins to appear from 80 W cm^{-2} and grows with laser flux. Quantitative analysis of the diffraction peaks provides detailed information on the perovskite films. Figure 2b shows full width at half-maximum (fwhm) of tetragonal $MAPbI_3$ (110) and (220) lattice peaks. The fwhm values of both peaks monotonically decrease with power density. Slight increase of the fwhm around 120 W cm^{-2} is attributed to decomposition of the perovskite structure. Figure 2c presents relative peak intensity ratios of intermediate phase (MAI−PbI_2−DMSO) peak at 9.3° and PbI_2 peak at 12.8° to perovskite (110) ($MAPbI_3$) peak at 14.2°. The relative portion of intermediate phase decreases with power density; particularly, it becomes negligible above 80 W cm^{-2}. The relative intensity of PbI_2 peak is noticeable from 80 W cm^{-2} and abruptly increases at 120 W cm^{-2}. Figure 2d illustrates the phase transformation model under laser irradiation. Along with power density, the poorly crystalline intermediate phase of the as-deposited film is transformed into a highly crystalline perovskite phase. Further increase in the laser power density over 120 W cm^{-2} greatly activates the decomposition of $MAPbI_3$ into PbI_2.[38−41]

Our analysis on surface temperature clarifies the underlying mechanism of phase transformation induced by NIR laser irradiation. As illustrated in Figure 3a, while the laser beam propagates through $MAPbI_3$ precursor layer, photothermal effect at ITO electrode and PEDOT:PSS charge transport layers contributes to an instantaneous local heating.[27] The

DOI: 10.1021/acsnano.6b03815
ACS Nano 2016, 10, 7907−7914

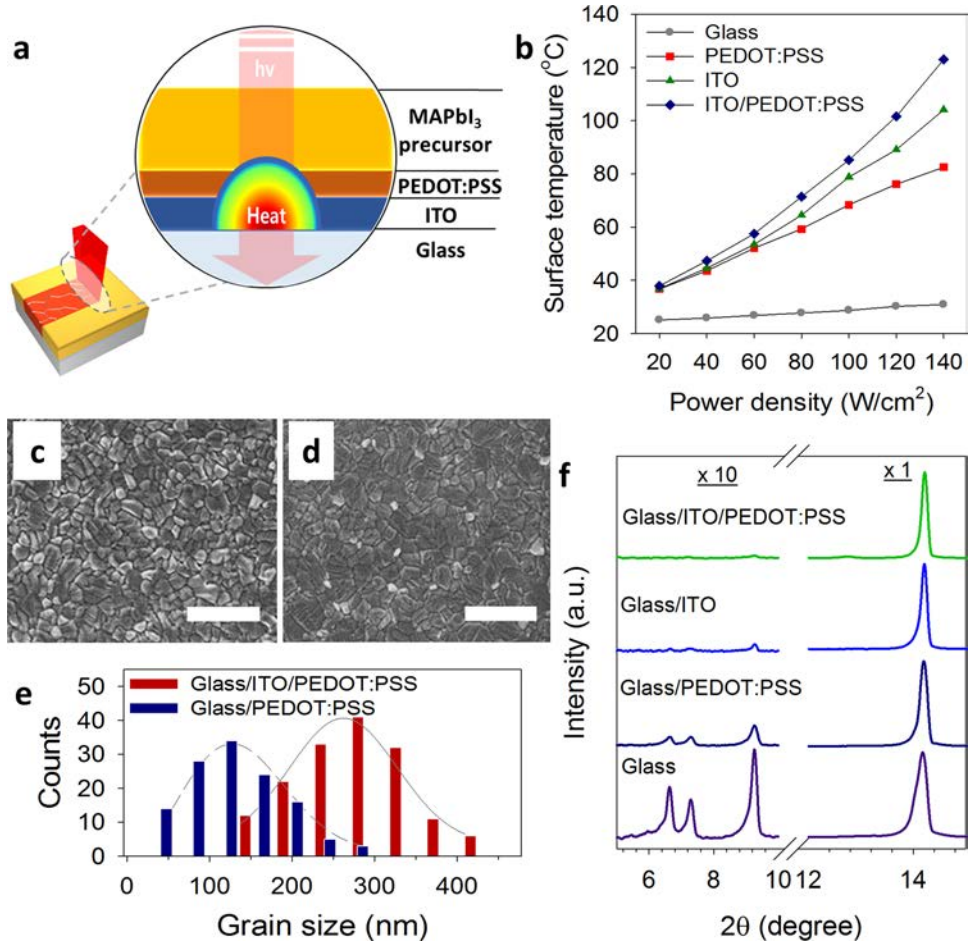

Figure 3. (a) Schematic illustration for photothermal heating. (b) Surface temperature of substrates with laser power density measured by IR thermal camera. SEM image of perovskite on (c) glass/PEDOT:PSS and (d) glass/ITO/PEDOT:PSS substrates (scale bar: 500 nm). (e) Grain size distributions of perovskites on two different substrates. (f) XRD patterns of laser-crystallized perovskites on different substrates with constant power density and scan rate of 80 W cm^{-2} and 0.1 mm s^{-1}, respectively.

surface temperature measured by IR thermal camera is plotted against laser power density in Figure 3b. Indeed, the degree of temperature increase strongly depends on the substrates and interfacial layers. ITO or PEDOT:PSS layer substantially absorbs laser and induces photothermal heating, while photothermal conversion of bare glass substrate is marginal. Free charge carriers in conductive ITO and PEDOT:PSS layer absorb the photon energy of laser beam.[42−44] This photoexcitation can be rapidly equilibrated to phonon vibration and trigger instantaneous local heating. ITO/PEDOT:PSS bilayer shows the highest temperature increase due to the synergetic effect from both layers. The typical photothermal heating temperature ranging from 30 to 120 °C is sufficient for the phase transformation of solution deposited perovskites.[45] Figures 3c and 3d compares the film morphology of laser crystallized perovskites on PEDOT:PSS and ITO/PEDOT:PSS layers, respectively. The film on ITO/PEDOT:PSS layer has a significantly larger average grain size (300 nm) than that on PEDOT:PSS (140 nm) (Figure 3e). XRD patterns also reveal a clear distinction in their crystallinities. Figure 3f compares the relative intensities of intermediate peaks normalized by perovskite (110) peaks. The film on ITO/PEDOT:PSS shows the lowest intermediate peak intensities and fwhm values (Figure S4).

Figure 4a inset depicts the device architecture of the laser crystallized inverted type solar cells used in this work. ITO anode, PEDOT:PSS hole transport layer, $MAPbI_3$ light absorbing layer, phenyl-C_{61}-butyric acid methyl ester ($PC_{61}BM$) electron transport layer, and calcium and aluminum cathode were sequentially deposited. It is noteworthy that despite the relatively low energy conversion efficiency around 10−14%,[45,46] this inverted device structure enables all solution processing of perovskite solar cells on conventional flexible polymer substrates. Current density−voltage (J−V) characteristics measured under standard air mass 1.5 global illuminations (AM 1.5G) are presented in Figure 4a. J−V curve strongly depends on the laser irradiation conditions. Short-circuit current (J_{sc}) substantially increases with laser power density. Large fill factors (FF) over 77% are recorded for the most of devices and reaches up to 80%, illustrating low leakage current. The highest PCE of 12.6% is attained for 80 W cm^{-2} laser power density with minimal hysteresis with 10 ms delay time (Figure S5). Typical solar cell parameters are summarized in Table 1.

For laser crystallized perovskite solar cells, J_{sc} is turned out to be the most critical parameter for PCE among solar cell parameters. Light absorption, carrier lifetime or carrier collection can be significantly influenced by the film morphology and crystallinity of laser crystallized perovskite

DOI: 10.1021/acsnano.6b03815
ACS Nano 2016, 10, 7907−7914

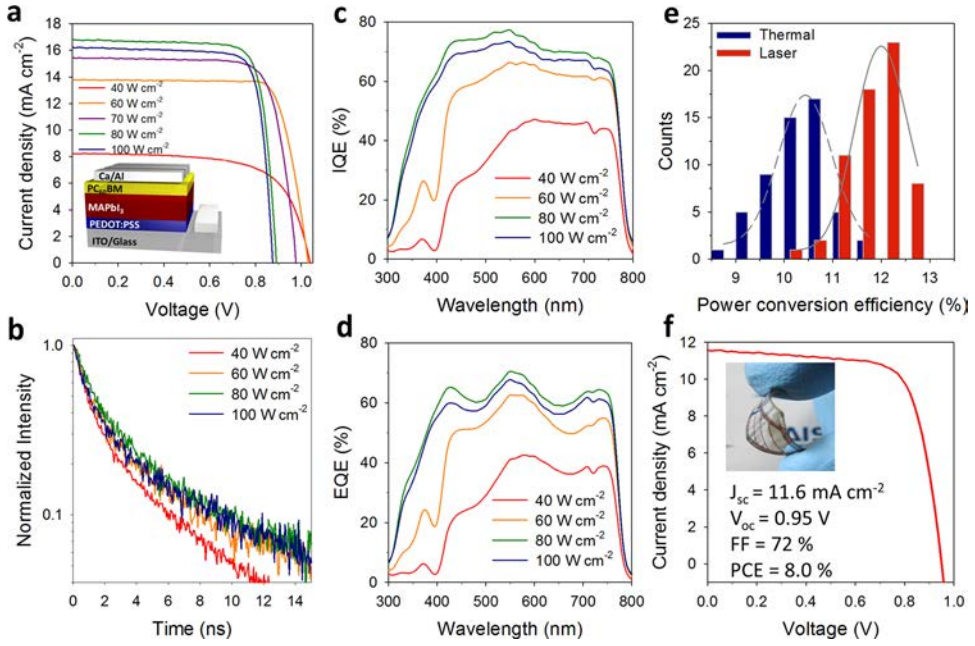

Figure 4. (a) Current density−voltage (J−V) characteristics of perovskite solar cells produced by various laser power densities under standard AM 1.5G condition (inset: scheme of device architecture). (b) Time resolved photoluminescence, (c) internal quantum efficiency, and (d) external quantum efficiency along with laser power density. (e) Power conversion efficiency distribution of perovskite solar cells based on conventional thermal annealing (100 °C for 5 min) and laser crystallization (80 W cm^{-2} and 0.1 mm s^{-1}). (f) J−V curve of a flexible solar cell fabricated on ITO coated PEN substrate (inset: photo of the flexible solar cell fabricated by employing the laser crystallization).

Table 1. Summary of Solar Cell Parameters with Different Laser Power Densities[a]

Power density (W cm^{-2})	V_{oc} (V)	J_{sc} (mA cm^{-2})	FF (%)	PCE best (%)	PCE average (%)
40	1.038	8.23	67.11	6.03	5.7
60	1.030	13.80	79.97	11.95	11.22
70	0.976	15.43	77.52	12.29	11.64
80	0.891	16.79	80.07	12.61	12.10
100	0.875	16.24	80.67	11.47	11.38
80-forward	0.910	14.47	79.60	11.23	
80-reverse	0.920	14.44	75.20	10.71	

[a]Figure 4a.

layer. Ultraviolet−visible absorption spectra of the $MAPbI_3$ layers are measured with different laser irradiation conditions (Figure S6a). All samples show absorption edge at 770−780 nm for typical $MAPbI_3$ perovskite. The distinctive absorption peak at 500 nm (observed over 100 W cm^{-2}) corresponds to the absorption by PbI_2 (Figure S6b). A 80 W cm^{-2} irradiation results in the highest absorption over the entire wavelength range. Although J_{sc} value is roughly proportional to the light absorption intensity, noticeably different J_{sc} values are observed despite the similar absorption intensities for 60 (J_{sc} = 13.80 mA cm^{-2}) and 100 W cm^{-2} (J_{sc} = 16.24 mA cm^{-2}) laser power densities. This signifies different charge carrier behaviors depending on laser irradiation conditions.

Perovskite crystalline morphology determined by laser crystallization also influences the charge carrier recombination and carrier lifetimes. Figure 4b presents time-resolved photoluminescence of laser-crystallized $MAPbI_3$ on glass/ITO/PEDOT:PSS substrates. A 40 W cm^{-2} radiated sample shows the fastest decay, whereas 80 W cm^{-2} shows the slowest decay in the normalized intensities. The decay curves are fitted with biexponential function and yield two different carrier lifetimes, τ_1 and τ_2, which are characteristics for bimolecular and radiative recombination, respectively (Table S1).[37] Both τ_1 and τ_2 increase along with laser power density from τ_1 = 0.9 ns and τ_2 = 6.3 ns (40 W cm^{-2}) to τ_1 = 1.60 ns and τ_2 = 13.4 ns (80 W cm^{-2}). Afterward, they slightly decrease down to τ_1 = 1.31 ns and τ_2 = 12.4 ns at 100 W cm^{-2}. Large grain size with pure crystalline structure leads to long lifetimes of charge carriers (Figure S3).

Figure 4c presents internal quantum efficiencies (IQEs) of perovskite solar cells as a function of laser power density. In the wavelength regime over 550 nm, IQEs show similar plateau behaviors for all laser irradiation conditions, whose relative magnitude is principally governed by carrier lifetime (Table S1).[4,47,48] By contrast, the curve shapes are strongly influenced by laser power in the short wavelength regime under 550 nm. In contrast to the optimized plateau behavior at 80 W cm^{-2}, a higher or lower laser power results in significantly reduced efficiency particularly below 450 nm. As short wavelength light is principally absorbed near the bottom PEDOT:PSS/$MAPbI_3$ interface (i.e., light incident through glass/ITO), photogenerated electrons should pass through the long transport pathway of perovskite layer to reach cathode (Ca/Al) and contribute to IQE. Poorly crystalline structure and grain boundaries in the perovskite layer (Figure S3) may hinder the charge transport, and thus, collection efficiency of photo-

DOI: 10.1021/acsnano.6b03815
ACS Nano 2016, 10, 7907−7914

generated charge carriers is lowered. Figure 4d presents the external quantum efficiencies (EQEs) of perovskite solar cells that comprises both light absorption characteristics and carrier collection efficiency.[49,50] Overall curve shapes are similar to IQEs, illustrating that effective collection of photogenerated charge carriers is dominant for overall EQEs. EQE reaches up to 70% at 550 nm with 80 W cm^{-2} laser power density, where J_{sc} is calculated to be 15.9 mA cm^{-2}. Figure 4e compares the statistical distribution of PCE values of perovskite solar cells fabricated by laser crystallization (80 W cm^{-2} and 0.1 mm s^{-1}, 62 cells) and conventional static thermal annealing (100 °C for 5 min, 54 cells). $J-V$ curves for the best performance solar cells are shown in Figure S7. For laser crystallization, more than half of the devices showed PCE over 12% and 95% of cells exhibited PCE over 11%. The average PCE of 12% obtained by curve fitting (gray solid line) for laser crystallized solar cells is noticeably higher than that of thermally crystallized ones (gray dash line, average PCE: 10.5%).

Laser crystallization of perovskite solar cells is highly compatible with continuous fast processing on flexible substrate geometry, which is a crucial demand for next generation flexible solar cells. We investigate the fast crystallization of perovskite solar cells with the maximum allowed power density of our homemade laser system (200 W cm^{-2}). High performance solar cells are fabricated without rigorous process optimization, presenting typical solar cell parameters of J_{sc} = 14.5 mA cm^{-2}, V_{oc} = 0.91 V, FF = 80%, and PCE = 11.3% with a scan rate of 6 mm s^{-1} (21 m hr^{-1}) (Figure S8). This fast processing is also successfully employed for commercial ITO-coated poly(ethylene-2,6-naphthalate) (PEN) substrates with the sheet resistance <15 ohm sq^{-1}. Figure 4f shows $J-V$ curve of a flexible perovskite solar cell fabricated using laser power density of 200 W cm^{-2} and scan rate of 17 mm s^{-1} (61 m hr^{-1}). PCE of 8.0% is achieved with J_{sc} = 11.6 mA cm^{-2}, V_{oc} = 0.95 V, and FF = 72%. It is noteworthy that the fast laser scanning speed used in this work is far higher than that of currently reported perovskite coating speed (1 to 5 mm s^{-1}).[51]

CONCLUSION

In summary, laser photothermal crystallization has been successfully implemented for organic–inorganic hybrid perovskite solar cells. Reliable controllability of perovskite crystalline structure and morphology with low energy NIR laser beam realizes high performance solar cells on flexible polymer as well as hard glass substrates. Remarkable processing speed of this method suggests a direct compatibility to practical roll-to-roll printing. Moreover, slit beams or beam arrays can be employed for the large-area parallel processing. Owing to the diverse functionalities of halide perovskites and relevant organic–inorganic hybrid materials, this beam-damage-free laser processing offers a platform for solution based manufacture of flexible/wearable electronics and optoelectronics.

EXPERIMENTAL METHODS

Materials. ITO-coated glass substrates (corning glass, 15 ohm sq^{-1}) were cleaned by ultrasonication with detergent, DI water, acetone, and 2-propanol and exposed to UV–ozone for 20 min. PEDOT:PSS (Clevios P VP. Al 4083) was purchased from Heraeus Holdings GmbH and used as received. For the synthesis of methylammonium lead iodide ($MAPbI_3$), methylammonium iodide (purity >98%) and lead(II) iodide (purity >99.999%) were purchased from Dyesol and Alfa Aesar, respectively, and used without further purification. Phenyl-C_{61}-butyric acid methyl ester ($PC_{61}BM$, purity 99.5%) was purchased from 1-material.

Device Fabrication. PEDOT:PSS were spin-coated on ITO at 5000 rpm for 30 s and annealed at 150 °C for 10 min. For perovskite layer formation, precursor solution was prepared by dissolving methylammonium iodide and lead(II) iodide with 1:1 molar ratio in mixed solvent of gamma-butyloractone (Aldrich) and dimethylsurfoxide (Aldrich) with 7:3 volume ratio at room-temperature. $MAPbI_3$ wet film was formed by nonsolvent dripping process during spin-coating of precursor solution at 3000 rpm for 55 s in a nitrogen-filled glovebox. Laser irradiation was carried out using homemade system based on Nd:YAG laser source with 1064 nm of wavelength.[52] Laser beam has a shape of ellipse with the major and minor axis diameters of 3 and 2 mm, respectively. $PC_{61}BM$ was spin-coated in the glovebox at 1000 rpm for 60 s without thermal annealing. Finally, calcium and aluminum were sequentially deposited by thermal evaporation. The active area of solar cells is 0.1 cm^2, which is known to have no significant efficiency overestimation associated with small cell area.[53,54]

Characterization. Morphology of perovskite film layer and solar cell devices was characterized by SEM (S-4800, Hitachi). X-ray diffractions of perovskite thin-films were obtained using Rigaku D/MAX-2500 (Cu Kα radiation, 40 kV, 300 mA). Absorbance spectra were recorded by UV–vis spectrometer (UV-3600, Shimadzu). Thermal camera (FLIR T460) was used to measure the surface temperature of glass substrates and ITO and/or PEDOT:PSS coated glass substrates. The temperature was calibrated by setting emissivity values of ε = 0.47 and 0.53 for ITO and PEDOT:PSS, respectively. Current–voltage characteristics of perovskite solar cells were measured using a solar simulator (Newport, ORIEL sol 1A) with a source meter (Keithley 2400) under AM 1.5G condition. Internal and external quantum efficiency was measured by ORIEL IQE-200 (Newport). Time-resolved photoluminescence was characterized by time-correlated single-photon counting (TCSPC) system (iHR320, Horiba Jobin Yvon Inc.).

ASSOCIATED CONTENT

Supporting Information

The Supporting Information is available free of charge on the ACS Publications website at DOI: 10.1021/acsnano.6b03815.

SEM images of laser crystallized $MAPbI_3$ perovskite by 1064 nm NIR laser, fwhm of perovskite (110) peak with substrates, hysteresis characteristics, absorbance of the perovskite films, summary of carrier lifetime, solar cell performance comparison of thermal or laser crystallized perovskite solar cells, solar cell performance with fast laser scan speed, SEM images of laser crystallized $MAPbI_3$ perovskite (808 and 532 nm lasers). (PDF)

AUTHOR INFORMATION

Corresponding Authors

*E-mail: byungha@kaist.ac.kr.
*E-mail: sangouk.kim@kaist.ac.kr.

Author Contributions

S.O.K. proposed the initial idea of this project; T.J. was responsible for entire experiments including device fabrication, characterization, and analysis; K.J.L. was responsible of laser system and gave advice for the system. H.M.J. and S.H.L. contributed laser system setting and carried our laser crystallization with T.J.; J.M.L., H.I.P., and M.K.K. contributed to the preparation of materials and samples. B.S. offered constructive advices on manuscript and analysis of device performance. S.O.K. and T.J. was responsible for managing all aspects of this project including the writing of manuscript.

Notes

The authors declare no competing financial interest.

DOI: 10.1021/acsnano.6b03815
ACS Nano 2016, 10, 7907–7914

ACKNOWLEDGMENTS

This work was supported by the National Creative Research Initiative (CRI) Center for Multi-Dimensional Directed Nanoscale Assembly (2015R1A3A2033061) and Global Frontier Program through the Global Frontier Hybrid Interface Materials (GFHIM) of the National Research Foundation of Korea (NRF) funded by the Ministry of Science, ICT & Future Planning (2013M3A6B1078874)

REFERENCES

(1) Cho, H.; Jeong, S. H.; Park, M. H.; Kim, Y. H.; Wolf, C.; Lee, C. L.; Heo, J. H.; Sadhanala, A.; Myoung, N.; Yoo, S.; Im, S. H.; Friend, R. H.; Lee, T. W. Overcoming the Electroluminescence Efficiency Limitations of Perovskite Light-Emitting Diodes. *Science* **2015**, *350*, 1222−5.

(2) Xing, G.; Mathews, N.; Lim, S. S.; Yantara, N.; Liu, X.; Sabba, D.; Grätzel, M.; Mhaisalkar, S.; Sum, T. C. Low-Temperature Solution-Processed Wavelength-Tunable Perovskites for Lasing. *Nat. Mater.* **2014**, *13*, 476−480.

(3) Burschka, J.; Pellet, N.; Moon, S.-J.; Humphry-Baker, R.; Gao, P.; Nazeeruddin, M. K.; Gratzel, M. Sequential Deposition as a Route to High-Performance Perovskite-Sensitized Solar Cells. *Nature* **2013**, *499*, 316−319.

(4) Jeon, N. J.; Noh, J. H.; Kim, Y. C.; Yang, W. S.; Ryu, S.; Seok, S. I. Solvent Engineering for High-Performance Inorganic-Organic Hybrid Perovskite Solar Cells. *Nat. Mater.* **2014**, *13*, 897−903.

(5) Yang, W. S.; Noh, J. H.; Jeon, N. J.; Kim, Y. C.; Ryu, S.; Seo, J.; Seok, S. I. High-Performance Photovoltaic Perovskite Layers Fabricated through Intramolecular Exchange. *Science* **2015**, *348*, 1234−1237.

(6) Im, J.-H.; Jang, I.-H.; Pellet, N.; Grätzel, M.; Park, N.-G. Growth of $CH_3NH_3PbI_3$ Cuboids with Controlled Size for High-Efficiency Perovskite Solar Cells. *Nat. Nanotechnol.* **2014**, *9*, 927−932.

(7) Lee, M. M.; Teuscher, J.; Miyasaka, T.; Murakami, T. N.; Snaith, H. J. Efficient Hybrid Solar Cells Based on Meso-Superstructured Organometal Halide Perovskites. *Science* **2012**, *338*, 643−647.

(8) Kim, H.; Lim, K.-G.; Lee, T.-W. Planar Heterojunction Organometal Halide Perovskite Solar Cells: Roles of Interfacial Layers. *Energy Environ. Sci.* **2016**, *9*, 12−30.

(9) Grinberg, I.; West, D. V.; Torres, M.; Gou, G.; Stein, D. M.; Wu, L.; Chen, G.; Gallo, E. M.; Akbashev, A. R.; Davies, P. K.; Spanier, J. E.; Rappe, A. M. Perovskite Oxides for Visible-Light-Absorbing Ferroelectric and Photovoltaic Materials. *Nature* **2013**, *503*, 509−512.

(10) Noh, J. H.; Im, S. H.; Heo, J. H.; Mandal, T. N.; Seok, S. I. Chemical Management for Colorful, Efficient, and Stable Inorganic−Organic Hybrid Nanostructured Solar Cells. *Nano Lett.* **2013**, *13*, 1764−1769.

(11) Hao, F.; Stoumpos, C. C.; Cao, D. H.; Chang, R. P.; Kanatzidis, M. G. Lead-Free Solid-State Organic-Inorganic Halide Perovskite Solar Cells. *Nat. Photonics* **2014**, *8*, 489−494.

(12) Shin, B.; Gunawan, O.; Zhu, Y.; Bojarczuk, N. A.; Chey, S. J.; Guha, S. Thin Film Solar Cell with 8.4% Power Conversion Efficiency Using an Earth-Abundant Cu_2ZnSnS_4 Absorber. *Prog. Photovoltaics* **2013**, *21*, 72−76.

(13) Green, M. A.; Ho-Baillie, A.; Snaith, H. J. The Emergence of Perovskite Solar Cells. *Nat. Photonics* **2014**, *8*, 506−514.

(14) Lin, Q.; Armin, A.; Nagiri, R. C. R.; Burn, P. L.; Meredith, P. Electro-Optics of Perovskite Solar Cells. *Nat. Photonics* **2014**, *9*, 106−112.

(15) Miyata, A.; Mitioglu, A.; Plochocka, P.; Portugall, O.; Wang, J. T.-W.; Stranks, S. D.; Snaith, H. J.; Nicholas, R. J. Direct Measurement of the Exciton Binding Energy and Effective Masses for Charge Carriers in Organic-Inorganic Tri-Halide Perovskites. *Nat. Phys.* **2015**, *11*, 582−587.

(16) D'Innocenzo, V.; Grancini, G.; Alcocer, M. J. P.; Kandada, A. R. S.; Stranks, S. D.; Lee, M. M.; Lanzani, G.; Snaith, H. J.; Petrozza, A. Excitons *versus* Free Charges in Organo-Lead Tri-Halide Perovskites. *Nat. Commun.* **2014**, *5*, 3586.

(17) Stranks, S. D.; Eperon, G. E.; Grancini, G.; Menelaou, C.; Alcocer, M. J. P.; Leijtens, T.; Herz, L. M.; Petrozza, A.; Snaith, H. J. Electron-Hole Diffusion Lengths Exceeding 1 Micrometer in an Organometal Trihalide Perovskite Absorber. *Science* **2013**, *342*, 341−344.

(18) Oga, H.; Saeki, A.; Ogomi, Y.; Hayase, S.; Seki, S. Improved Understanding of the Electronic and Energetic Landscapes of Perovskite Solar Cells: High Local Charge Carrier Mobility, Reduced Recombination, and Extremely Shallow Traps. *J. Am. Chem. Soc.* **2014**, *136*, 13818−13825.

(19) Kojima, A.; Teshima, K.; Shirai, Y.; Miyasaka, T. Organometal Halide Perovskites as Visible-Light Sensitizers for Photovoltaic Cells. *J. Am. Chem. Soc.* **2009**, *131*, 6050−6051.

(20) Jeon, N. J.; Noh, J. H.; Yang, W. S.; Kim, Y. C.; Ryu, S.; Seo, J.; Seok, S. I. Compositional Engineering of Perovskite Materials for High-Performance Solar Cells. *Nature* **2015**, *517*, 476−480.

(21) Wang, Q.; Shao, Y.; Dong, Q.; Xiao, Z.; Yuan, Y.; Huang, J. Large Fill-Factor Bilayer Iodine Perovskite Solar Cells Fabricated by a Low-Temperature Solution-Process. *Energy Environ. Sci.* **2014**, *7*, 2359−2365.

(22) Heo, J. H.; Im, S. H.; Noh, J. H.; Mandal, T. N.; Lim, C.-S.; Chang, J. A.; Lee, Y. H.; Kim, H.-j.; Sarkar, A.; Nazeeruddin, Md. K.; Gratzel, M.; Seok, S. I. Efficient Inorganic-Organic Hybrid Heterojunction Solar Cells Containing Perovskite Compound and Polymeric Hole Conductors. *Nat. Photonics* **2013**, *7*, 486−491.

(23) Liu, D.; Kelly, T. L. Perovskite Solar Cells with a Planar Heterojunction Structure Prepared Using Room-Temperature Solution Processing Techniques. *Nat. Photonics* **2013**, *8*, 133−138.

(24) Liu, M.; Johnston, M. B.; Snaith, H. J. Efficient Planar Heterojunction Perovskite Solar Cells by Vapour Deposition. *Nature* **2013**, *501*, 395−398.

(25) Lim, K.-G.; Kim, H.-B.; Jeong, J.; Kim, H.; Kim, J. Y.; Lee, T.-W. Boosting the Power Conversion Efficiency of Perovskite Solar Cells Using Self-Organized Polymeric Hole Extraction Layers with High Work Function. *Adv. Mater.* **2014**, *26*, 6461−6466.

(26) Lim, K.-G.; Ahn, S.; Kim, Y.-H.; Qi, Y.; Lee, T.-W. Universal Energy Level Tailoring of Self-Organized Hole Extraction Layers in Organic Solar Cells and Organic-Inorganic Hybrid Perovskite Solar Cells. *Energy Environ. Sci.* **2016**, *9*, 932−939.

(27) Grigoropoulos, C. P. *Transport in Laser Microfabrication: Fundamentals and Applications*; Cambridge University Press: New York, 2009.

(28) Tan, K. W.; Jung, B.; Werner, J. G.; Rhoades, E. R.; Thompson, M. O.; Wiesner, U. Transient Laser Heating Induced Hierarchical Porous Structures from Block Copolymer−Directed Self-Assembly. *Science* **2015**, *349*, 54−58.

(29) Im, J. S.; Kim, H.; Thompson, M. O. Phase Transformation Mechanisms Involved in Excimer Laser Crystallization of Amorphous Silicon Films. *Appl. Phys. Lett.* **1993**, *63*, 1969−1971.

(30) Thompson, M. O.; Galvin, G.; Mayer, J.; Peercy, P.; Poate, J.; Jacobson, D.; Cullis, A.; Chew, N. Melting Temperature and Explosive Crystallization of Amorphous Silicon During Pulsed Laser Irradiation. *Phys. Rev. Lett.* **1984**, *52*, 2360.

(31) Cottrell, T. L. *The Strengths of Chemical Bonds*, 2nd ed.; Butterworths Scientific Publications: London, 1958.

(32) Blanksby, S. J.; Ellison, G. B. Bond Dissociation Energies of Organic Molecules. *Acc. Chem. Res.* **2003**, *36*, 255−263.

(33) Niu, G.; Li, W.; Meng, F.; Wang, L.; Dong, H.; Qiu, Y. Study on the Stability of $CH_3NH_3PbI_3$ Films and the Effect of Post-Modification by Aluminum Oxide in All-Solid-State Hybrid Solar Cells. *J. Mater. Chem. A* **2014**, *2*, 705−710.

(34) Legeay, G.; Castel, X.; Benzerga, R.; Pinel, J. Excimer Laser Beam/ITO Interaction: From Laser Processing to Surface Reaction. *Phys. Status Solidi C* **2008**, *5*, 3248−3254.

(35) Sandmann, A.; Notthoff, C.; Winterer, M. Continuous Wave Ultraviolet-Laser Sintering of Zno and TiO2 Nanoparticle Thin Films at Low Laser Powers. *J. Appl. Phys.* **2013**, *113*, 044310.

DOI: 10.1021/acsnano.6b03815
ACS Nano 2016, 10, 7907−7914

(36) Li, B.-j.; Zhou, M.; Ma, M.; Zhang, W.; Tang, W.-y. Effects of Nanosecond Laser Irradiation on Photoelectric Properties of AZO/FTO Composite Films. *Appl. Surf. Sci.* **2013**, *265*, 637−641.
(37) Chen, Q.; Zhou, H.; Song, T.-B.; Luo, S.; Hong, Z.; Duan, H.-S.; Dou, L.; Liu, Y.; Yang, Y. Controllable Self-Induced Passivation of Hybrid Lead Iodide Perovskites toward High Performance Solar Cells. *Nano Lett.* **2014**, *14*, 4158−4163.
(38) Cheng, Y.; Yang, Q.-D.; Xiao, J.; Xue, Q.; Li, H.-W.; Guan, Z.; Yip, H.-L.; Tsang, S.-W. Decomposition of Organometal Halide Perovskite Films on Zinc Oxide Nanoparticles. *ACS Appl. Mater. Interfaces* **2015**, *7*, 19986−19993.
(39) Stoumpos, C. C.; Malliakas, C. D.; Kanatzidis, M. G. Semiconducting Tin and Lead Iodide Perovskites with Organic Cations: Phase Transitions, High Mobilities, and near-Infrared Photoluminescent Properties. *Inorg. Chem.* **2013**, *52*, 9019−9038.
(40) Song, T.-B.; Chen, Q.; Zhou, H.; Luo, S.; Yang, Y. M.; You, J.; Yang, Y. Unraveling Film Transformations and Device Performance of Planar Perovskite Solar Cells. *Nano Energy* **2015**, *12*, 494−500.
(41) Frost, J. M.; Butler, K. T.; Brivio, F.; Hendon, C. H.; van Schilfgaarde, M.; Walsh, A. Atomistic Origins of High-Performance in Hybrid Halide Perovskite Solar Cells. *Nano Lett.* **2014**, *14*, 2584−2590.
(42) Herrmann, F.; Engmann, S.; Presselt, M.; Hoppe, H.; Shokhovets, S.; Gobsch, G. Correlation between near Infrared-Visible Absorption, Intrinsic Local and Global Sheet Resistance of Poly(3,4-Ethylenedioxy-Thiophene) Poly(Styrene Sulfonate) Thin Films. *Appl. Phys. Lett.* **2012**, *100*, 153301.
(43) Haug, H.; Koch, S. W. *Quantum Theory of the Optical and Electronic Properties of Semiconductors*; World Scientific: Singapore, 1990; Vol. *5*.
(44) Singh, J. *Optical Properties of Condensed Matter and Applications*; John Wiley & Sons: Hoboken, NJ, 2006; Vol. *6*.
(45) Jung, J. W.; Williams, S. T.; Jen, A. K. Y. Low-Temperature Processed High-Performance Flexible Perovskite Solar Cells *via* Rationally Optimized Solvent Washing Treatments. *RSC Adv.* **2014**, *4*, 62971−62977.
(46) Seo, J.; Park, S.; Chan Kim, Y.; Jeon, N. J.; Noh, J. H.; Yoon, S. C.; Seok, S. I. Benefits of Very Thin PCBM and LiF Layers for Solution-Processed P-I-N Perovskite Solar Cells. *Energy Environ. Sci.* **2014**, *7*, 2642−2646.
(47) Park, H. I.; Lee, S.; Lee, J. M.; Nam, S. A.; Jeon, T.; Han, S. W.; Kim, S. O. High Performance Organic Photovoltaics with Plasmonic-Coupled Metal Nanoparticle Clusters. *ACS Nano* **2014**, *8*, 10305−10312.
(48) Shin, B.; Zhu, Y.; Bojarczuk, N. A.; Jay Chey, S.; Guha, S. Control of an Interfacial $MoSe_2$ Layer in $Cu_2ZnSnSe_4$ Thin Film Solar Cells: 8.9% Power Conversion Efficiency with a Tin Diffusion Barrier. *Appl. Phys. Lett.* **2012**, *101*, 053903.
(49) Lee, J. M.; Kwon, B.-H.; Park, H. I.; Kim, H.; Kim, M. G.; Park, J. S.; Kim, E. S.; Yoo, S.; Jeon, D. Y.; Kim, S. O. Exciton Dissociation and Charge-Transport Enhancement in Organic Solar Cells with Quantum-Dot/N-Doped Cnt Hybrid Nanomaterials. *Adv. Mater.* **2013**, *25*, 2011−2017.
(50) Lim, K.-G.; Ahn, S.; Kim, H.; Choi, M.-R.; Huh, D. H.; Lee, T.-W. Self-Doped Conducting Polymer as a Hole-Extraction Layer in Organic−Inorganic Hybrid Perovskite Solar Cells. *Adv. Mater. Interfaces* **2016**, *3*, 1500678.
(51) Hwang, K.; Jung, Y.-S.; Heo, Y.-J.; Scholes, F. H.; Watkins, S. E.; Subbiah, J.; Jones, D. J.; Kim, D.-Y.; Vak, D. Toward Large Scale Roll-to-Roll Production of Fully Printed Perovskite Solar Cells. *Adv. Mater.* **2015**, *27*, 1241−1247.
(52) Jin, H. M.; Lee, S. H.; Kim, J. Y.; Son, S.-W.; Kim, B. H.; Lee, H. K.; Mun, J. H.; Cha, S. K.; Kim, J. S.; Nealey, P. F.; Lee, K. J.; Kim, S. O. Laser Writing Block Copolymer Self-Assembly on Graphene Light-Absorbing Layer. *ACS Nano* **2016**, *10*, 3435−3442.
(53) Vendra, V. K.; Absher, J.; Ellis, S. R.; Amos, D. A.; Druffel, T.; Sunkara, M. K. Photoanode Area Dependent Efficiency and Recombination Effects in Dye-Sensitized Solar Cells. *J. Electrochem. Soc.* **2012**, *159*, H728.
(54) Manor, A.; Katz, E. A.; Tromholt, T.; Hirsch, B.; Krebs, F. C. Origin of size effect on efficiency of organic photovoltaics. *J. Appl. Phys.* **2011**, *109*, 074508.

DOI: 10.1021/acsnano.6b03815
ACS Nano 2016, 10, 7907−7914